Numerical Analysis and Experimental Study of Hard Roofs in Fully Mechanized Mining Faces under Sleeve Fracturing

Zhitao Zheng [1], Ying Xu [1],*, Desheng Li [1] and Jianghui Dong [2],*

Received: 2 September 2015 ; Accepted: 10 November 2015 ; Published: 20 November 2015
Academic Editor: Samuel Frimpong

[1] School of Civil Engineering and Architecture, Anhui University of Science and Technology, Huainan 232001, China; zztzheng@126.com (Z.Z.); lesary@163.com (D.L.)

[2] School of Natural and Built Environments, University of South Australia, Adelaide, SA 5095, Australia

* Correspondence: yxu@aust.edu.cn (Y.X.); Jianghui.Dong@unisa.edu.au (J.D.);
Tel./Fax: +86-0554-6668-749 (Y.X.); +61-883-023-068 (J.D.)

Abstract: Sudden falls of large-area hard roofs in a mined area release a large amount of elastic energy, generate dynamic loads, and cause disasters such as impact ground pressure and gas outbursts. To address these problems, in this study, the sleeve fracturing method (SFM) was applied to weaken a hard roof. The numerical simulation software FLAC^{3D} was used to develop three models based on an analysis of the SFM working mechanism. These models were applied to an analysis of the fracturing effects of various factors such as the borehole diameter, hole spacing, and sleeve pressure. Finally, the results of a simulation were validated using experiments with similar models. Our research indicated the following: (1) The crack propagation directions in the models were affected by the maximum principal stress and hole spacing. When the borehole diameter was fixed, the fracturing pressure increased with increasing hole spacing. In contrast, when the fracturing pressure was fixed, the fracturing range increased with increasing borehole diameter; (2) The most ideal fracturing effect was found at a fracturing pressure of 17.6 MPa in the model with a borehole diameter of 40 mm and hole spacing of 400 mm. The results showed that it is possible to regulate the falls of hard roofs using the SFM. This research may provide a theoretical basis for controlling hard roofs in mining.

Keywords: sleeve fracturing method; hard roof; impact ground pressure; deep mines

1. Introduction

Hard roofs in mining areas may generate very strong pressures. Their dynamic load coefficient may reach 3.5, with maximum pressure spacing as large as 160 m. The suspended roof area may range from 10,000 to 30,000 m^2, or even larger. The maximum edge length of falling rocks can reach 40 m, whereas the maximum height of the roof can be as large as 70 m [1–4]. In the mining process, a high pressure load on the roof control area of a fully mechanized mining face (FMMF) can seriously damage the FMMF support structures if no timely and effective measures are taken to regulate the fall of the hard roof. This high pressure load may also easily cause a hurricane or impact ground pressure, which leads to accidents, including serious damage to equipment, heavy mining staff casualties, and instantaneous outbursts of accumulated gas in the mined areas [5–9].

In recent years, with the increase in mining depth, the weakening of the hard roofs of FMMFs has been a topic of great interest among scholars around the world. The results from a large number of related studies have also been reported. Konicek *et al.* [10–13] pointed out that sudden falls of large-area hard roofs could release large amounts of elastic energy, generate dynamic loads, and

easily cause impact ground pressure disasters. They stated that long-hole blasting could be used to regulate the falls of hard roofs to avoid impact ground pressure disasters. Ito and Hayashi [14] proposed a new theory of stress measurement in hydraulic fracturing. They cracked cubic rock samples using the hydraulic fracturing method in a laboratory. Their results could be applied to controlling hard roofs in mining. Fan *et al.* [15] studied the mechanism of the directional hydraulic fracturing of hard roofs using theoretical analysis and numerical simulation. They applied the method to weaken the hard roof of the 6305 working face in the No. 3 Mine of Jining, China. Their results indicated that the directional hydraulic fracturing method can effectively weaken hard roofs and is simple and safe to implement compared with the blasting method. Wang *et al.* [16] determined the falling mechanism of hard roofs and reasonable blasting parameters after establishing a long-hole pre-splitting blasting model using the LS-DYNA software based on the field conditions of the hard roofs for shallow buried coal seams. The authors used field experiments to demonstrate that the long-hole pre-splitting blasting method could be used to effectively control the falls of hard roofs. Huang *et al.* [17] adopted a linear porous hydraulic fracturing method and long-hole inclined hydraulic fracturing method to control the fall of thick hard roofs. Their method did not use blasting. In addition, it ensured a safe and efficient mining operation. The method was simple, safe and cost-effective compared with blasting and traditional hydraulic fracturing. Wang *et al.* [18] noted that the sudden falls of roofs covered with hard thick sandstone at extreme heights may easily lead to disasters such as gas outbursts and impact ground pressure. The falling span range of hard thick sandstone roofs can be reduced using hydraulic fracturing, and gas outbursts can be prevented using gas drainage technology. Li *et al.* [19] proposed a dynamic and static press crushing mechanism with rock blasting to address the hard roof problem. They used the software AUTODYN to conduct numerical simulations of drilling and blasting. The blasting effect of using decoupled charges in the blast holes was analyzed according to the rupture process of single-hole and two-hole rock blasting. Their results showed that the dynamic and static press method was an effective and feasible way to weaken hard roofs. He *et al.* [20] applied directional hydraulic fracturing technology to weaken the hard roofs of mines. An initial notch was made inside each borehole before injecting high-pressure water. Rocks were cracked by the action of this high-pressure water, which prevented impact ground pressure disasters from the sudden fall of hard roofs.

It can be seen from the results of previous studies that it is necessary to change the physical and mechanical properties of roofs to effectively control the falls of hard roofs in mined areas. The hanging exposed area must be reduced to prevent impact pressure on large-area roofs. There are currently two methods to accomplish this: weakening by high-pressure water and blasting [21,22]. Weakening by blasting results in significant cracking effects, with a wide fracturing range and high fracturing efficiency [12,20]. However, the extensive use of explosives will contaminate the underground environment of a mine, and strong blasting shocks will loosen the surrounding rocks. In the case of shallow-depth coal seams, inadequate blasting control will also cause a threat to the safety of the ground and the surrounding environment. Conducting such operations in gas-rich regions is very dangerous. Any carelessness can result in a gas explosion, coal seam collapse, and other major problems. Weakening by injecting high-pressure water is widely used in the oil and natural gas industries, and this method has a wide range of industrial applications. It is safe, has no impact on the working face, and does not pollute the mining environment [23,24]. However, the effect of fracturing when applying this method is influenced by factors that include the joint condition, mineral composition, and cementation of the roof rocks. The weakening of the roof requires a certain period of time. Therefore, this weakening method is not suitable when the working schedules are very tight.

To compensate for the shortcomings of the two common methods described, the sleeve fracturing method (SFM) was applied to the weakening of hard roofs in mines. Based on the sleeve fracturing mechanism, the simulation software FLAC^{3D} was used to establish numerical models. Analyses were conducted using the borehole diameter, hole spacing, and sleeve pressure, and the relationships between them were obtained. At the same time, a similar model experiment was designed to validate

the results of the simulation. Finally, the optimal parameters for cracking hard roofs were obtained for the sleeve fracturing process by analyzing the crack propagation in the model destruction process and the influence factors for the sleeve fracturing effects. The findings of this study may provide a theoretical basis for controlling the hard roofs in mines.

2. Mathematical Model of Sleeve-Fracturing Hard Roof

Currently, the SFM is primarily used for measurements of ground stress, rock shear, tensile strength, *etc.* It has rarely been applied in the research on the weakening of hard roofs in mines [25,26]. In this method, a rubber sleeve is used as the main working body. By connecting a high-strength pipeline and power system, the internal oil pressure in the hoisting process is transmitted to the sidewall of a borehole, which causes it to fracture. This changes the physical and mechanical properties of roofs and causes the fall of hard roofs in mined areas. The working mechanisms for the sleeve fracturing of hard roofs are mainly divided into single-hole controlled fracturing and multi-hole controlled fracturing [27–29].

2.1. Working Mechanism of Single-Hole Controlled Fracturing

Based on the differences in the crack directions, the working mechanisms for single-hole controlled fracturing can be divided into two-way controlled fracturing (TCF) and unidirectional controlled fracturing (UCF). In the case of TCF, a circumferential stress is applied to the sidewall surface of a single borehole through a high-pressure rubber sleeve tube. A fracturing experiment is conducted to cause the cracking of a single borehole. The fracturing pressure is used to obtain the first and third principal stresses (σ_1 and σ_3) in the plane of the normal direction. In the case of UCF, two semicircular cavities are used to apply pressure on the sidewall of the hole. The largest tangential stress on the sidewall of the hole is found in the gap between the two shells, which makes it possible to use a concentrated stress to control the crack extension in one direction.

2.1.1. Working Mechanism of Single-Hole Two-Way Controlled Fracturing (TCF)

Under the premise of no initial crack, the first crack in the borehole sidewall appears when the tangential stress of the borehole sidewall is greater than the tensile strength of the rock. The tangential stress consists of two parts: the original rock stress around the borehole and the sleeve pressure. The superposition of these two varies with the nature of the medium [25,26,30].

When $\theta = 0°$,

$$\sigma_{\theta 0} = 3\sigma_3 - \sigma_1 - P \tag{1}$$

When $\theta = 90°$,

$$\sigma_{\theta 90} = 3\sigma_1 - \sigma_3 - P \tag{2}$$

where θ is the angle of intersection with the first principal stress, σ_1 is the first principal stress, σ_3 is the third principal stress, P is the internal circumferential pressure, $\sigma_{\theta 0}$ is the tangential stress value at $\theta = 0°$, and $\sigma_{\theta 90}$ is the tangential stress value at $\theta = 90°$.

A continuous load was applied to the rock through the rubber sleeve. Two cracks orthogonal to each other appeared around the first crack, as shown in Figure 1a. The following two equations were obtained through an analysis of the initial propagation of these cracks [25,26]:

For cracks at $\theta = 0°$,

$$\sigma_{\theta 0} = T = 3\sigma_3 - \sigma_1 - P_1^C \tag{3}$$

For cracks at $\theta = 90°$,

$$\sigma_{\theta 90} = T = 3\sigma_1 - \sigma_3 - P_2^C \tag{4}$$

where θ is the angle of intersection with the first principal stress, σ_1 is the first principal stress, σ_3 is the third principal stress, P_1^C is the circumferential pressure at $\theta = 0°$, P_2^C is the circumferential pressure at $\theta = 90°$ when cracks were formed, and T is the tensile strength of the rock.
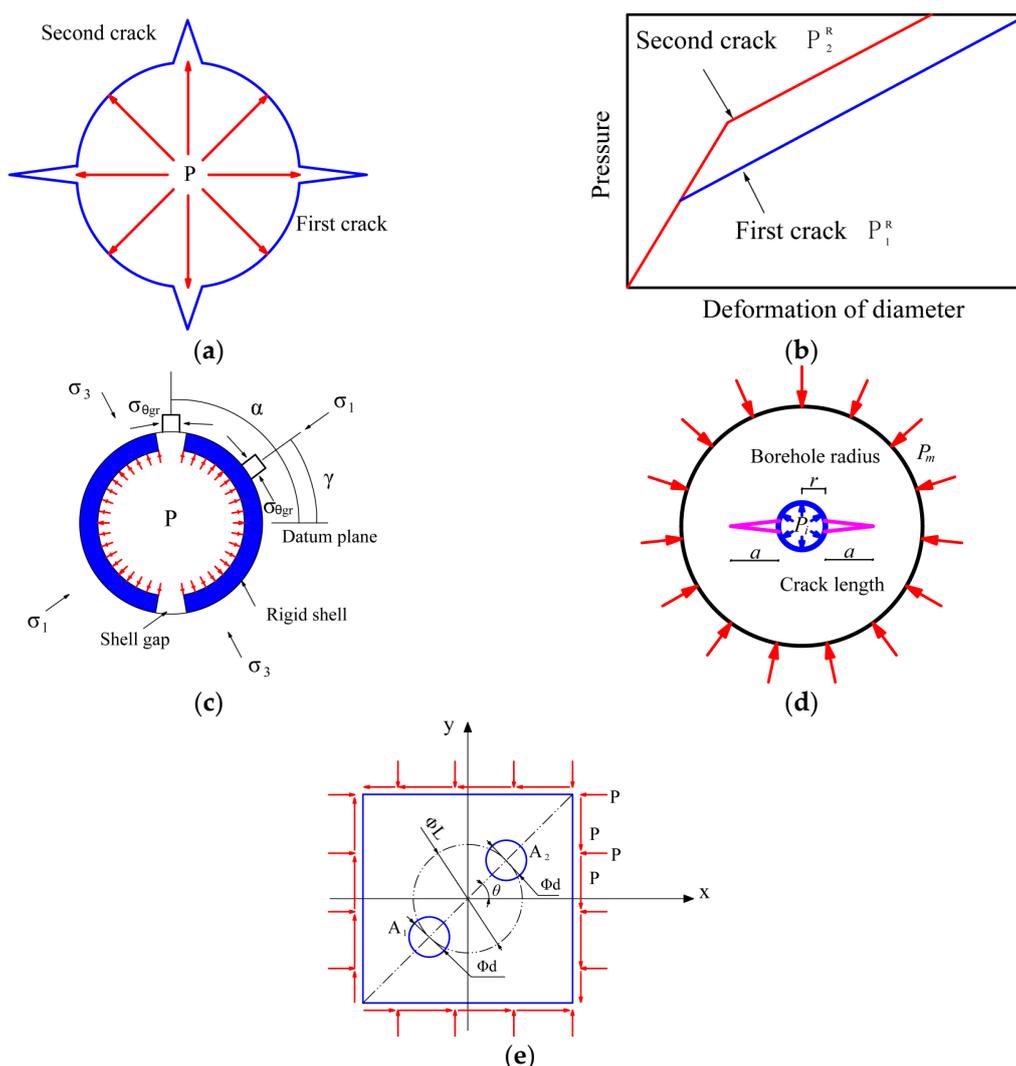
Figure 1. Working principle of sleeve fracturing. (**a**) Propagation of two-way crack; (**b**) Relationship between fracture and diameter in two-way crack; (**c**) Shear stress on wall in unidirectional crack; (**d**) Superposition of borehole stress intensity; (**e**) Drilling layout.

After unloading, reloading will further expand the cracks in the borehole sidewall. At $\theta = 0°$, the re-expanding stress at the crack is found as follows [25,26,30]:

$$\sigma_{\theta 0} = T = 3\sigma_3 - \sigma_1 - P_1^R \tag{5}$$

At $\theta = 90°$, the re-expanding stress at the crack is found as follows [25,26,30]:

$$\sigma_{\theta 90} = T = 3\sigma_1 - \sigma_3 - P_2^R \tag{6}$$

where P_1^R is the circumferential pressure at $\theta = 0°$ when cracks re-expand, and P_2^R is the circumferential pressure at $\theta = 90°$ when cracks re-expand.

By combining Equations (5) and (6), the following equations are obtained:

$$\sigma_1 = (P_1 + 3P_2)/8 \tag{7}$$

$$\sigma_3 = (3P_1 + P_2)/8 \tag{8}$$

The relationship curves between the stress and borehole diameter for the two loading processes are shown in Figure 1b. σ_1 and σ_3 can be obtained by substituting the resulting re-expanding pressures P_1^R and P_2^R of each fracture into Equations (7) and (8), respectively.

2.1.2. Working Mechanism of Single-Hole Unidirectional Controlled Fracturing (UCF)

In single-hole UCF, a load is applied on the borehole sidewall through two semicircular rigid shells on the probe surface of the fracturing device (see Figure 1c). The values of tangential stress on the borehole sidewall reach a maximum in the gaps between the two shells. The stress is concentrated to control the expansion of the cracking in one direction and fracture the rocks. The tangential stress at the time of crack appearance satisfies the following equation [26,30]:

$$\sigma_{\theta gr} = \sigma_3 + \sigma_1 + 2(\sigma_3 - \sigma_1)\cos2(\alpha - \gamma) - 1.79P \tag{9}$$

where $\sigma_{\theta gr}$ is the tangential stress in the gap, α is the inclination angle of the gap to the reference plane, γ is the inclination angle of σ_1 to the reference plane, and P is the circumferential pressure on the rigid shells.

According to the theory of fracture mechanics, in an infinite plane, the stress around a borehole P_m and sleeve pressure P_i will be superposed at the borehole, as shown in Figure 1d.

In the infinite plane, let the borehole radius be r, with two cracks of length a formed in the borehole radial direction under the combined effect of the stress around the borehole P_m and the sleeve pressure P_i. By introducing the stress intensity factor K_I, various types of stresses are superposed at the borehole (Figure 1d), and the following relationships are obtained [29–31]:

$$K_I(P_m) = P_m\sqrt{r} \times f_{P_m}(a,r) \tag{10}$$

$$K_I(P_i) = P_i\sqrt{r} \times f_{P_i}(a,r) \tag{11}$$

$$f_{P_m}(a,r) = 2\left(1 + \frac{a}{r}\right)^2 \left(\frac{\left(1 + \frac{a}{r}\right)^2 - 1}{\left(\pi\left(1 + \frac{a}{r}\right)\right)^7}\right)^{\frac{1}{2}} + \left(\pi\left(1 + \frac{a}{r}\right)\right)^{\frac{1}{2}}\left(1 - \frac{2}{\pi}\sin^{-1}\frac{1}{1 + \frac{a}{r}}\right) \tag{12}$$

$$f_{P_i}(a,r) = \left(1.3\frac{\frac{a}{r}}{1 + \left(1 + \frac{a}{r}\right)^{\frac{3}{2}}} + \left(\frac{7.8\left(\sin\left(\frac{2a}{r}\right)\right)}{2\left(1 + \frac{a}{r}\right)^{\frac{5}{2}} - 1.7}\right)\right) \tag{13}$$

Therefore, the total stress at the borehole $K_{IC} = K_I(P_m) + K_I(P_i)$ when the borehole cracks.

2.2. Working Mechanism of Multi-Hole Controlled Fracturing

When two boreholes of diameter d are located on a circle of diameter L, the line connecting the two borehole centers passes through the center of the circle at an inclination angle θ to the horizontal axis (Figure 1e). With consideration given to the effects of the initial rock stress, the far boundaries of the borehole are affected by the stresses σ_x, σ_y and τ_{xy}. When a load is applied inside the borehole and exceeds a certain limit, a crack will first appear along the line connecting the two borehole centers. This limit is the burst pressure P_{b1}. Here, the tangential stress σ_θ generated under the combined effect of the burst pressure P_{b1} and the original rock stress on the borehole sidewall is equal to the tensile strength of the rock T, and the following relationship holds true [26,31]:

$$P_{b1} = \sigma_x + \sigma_y - 2(\sigma_x - \sigma_y)\cos2\theta - 4\tau_{xy}\sin2\theta + T \tag{14}$$

Because of the appearance of the first crack, repeated fracturing in the multi-hole fracturing model does not need to overcome the tensile strength of the rock T among the holes, *i.e.*, $T = 0$. Substituting $T = 0$ into Equation (14) results in the second burst pressure P_{b2}, as follows [26,31]:

$$P_{b2} = \sigma_x + \sigma_y - 2(\sigma_x - \sigma_y)\cos2\theta - 4\tau_{xy}\sin2\theta \qquad (15)$$

To determine the three components of the original rock stress in Equation (15), it is necessary to conduct controlled fracturing experiments in the three directions (θ_1, θ_2, θ_3). The three resultant burst pressures are recorded as P_{b2}', P_{b2}'' and P_{b2}'''. The following linear algebraic equations are established with the original rock stresses σ_x, σ_y and τ_{xy} as unknowns [26,31]:

$$\begin{cases} f_{11}\sigma_x + f_{21}\sigma_y + f_{32}\tau_{xy} = P_{b2}' \\ f_{12}\sigma_x + f_{22}\sigma_y + f_{32}\tau_{xy} = P_{b2}'' \\ f_{13}\sigma_x + f_{23}\sigma_y + f_{33}\tau_{xy} = P_{b2}''' \end{cases} \qquad (16)$$

where $f_{1i} = 1 - 2\cos2\theta_i$, $f_{2i} = 1 + 2\cos2\theta_i$ and $f_{3i} = -4\sin2\theta_i$, i =1, 2, 3.

$$\begin{cases} \sigma_1 = \frac{1}{2}(\sigma_x + \sigma_y) + \frac{1}{2}\sqrt{(\sigma_x - \sigma_y)^2 + 4\tau_{xy}{}^2} \\ \sigma_3 = \frac{1}{2}(\sigma_x + \sigma_y) - \frac{1}{2}\sqrt{(\sigma_x - \sigma_y)^2 + 4\tau_{xy}{}^2} \\ \alpha = \frac{1}{2}\text{arctg}\frac{2\tau_{xy}}{\sigma_x - \sigma_y} \end{cases} \qquad (17)$$

After solving for the original rock stresses σ_x, σ_y and τ_{xy}, Equations (16) and (17) can be combined to derive the maximum principal stress, minimum principal stress, and direction of the principal stress.

In the process of multi-hole controlled fracturing, when $\sigma_1/\sigma_3 \approx 1$, the development of an expansive crack in the borehole is not restrained by the stress state, and the direction of the principal stress may change arbitrarily. When $\sigma_1/\sigma_3 \geqslant 1.5$, the development of an expansive crack in the borehole is difficult to control, and the inclination angle between the lines parallel to the line connecting the two borehole centers and the direction of the maximum principal stress becomes larger. In addition, an expansive crack in the borehole in a multi-hole controlled fracturing experiment primarily develops along the line connecting two borehole centers, *i.e.*, the direction of the row of holes.

3. Simulation of Cracking Roofs with SFM (Sleeve Fracturing Method)

3.1. Model Establishment

FLAC^{3D} (CnTech Co. Ltd, Shanghai, China) was used to establish three-dimensional models of hard roofs in an FMMF. The shell unit was used to generate the high-pressure rubber sleeve [32,33]. The model parameters were 700 mm × 300 mm × 400 mm (Length × Width × Heigth), and the borehole depth was 200 mm. The model was divided into 71,800 units with 73,950 nodes, and the model grid is shown in Figure 2.

To investigate the relationships between the borehole diameter, hole spacing, and fracturing pressure, the model was first divided into three groups with values of 20, 30 and 40 mm for borehole diameter d. In each group, the hole spacing took the three values of 5d, 8d and 10d. In the simulation, the model was regarded as a rock with homogenous properties by ignoring several factors such as the rheological behavior of the surrounding rock, joints in the rock, cracks, and the influence of water. The physical and mechanical parameters of the rock were given values that were 1/10 those of sandstone, as listed in Table 1.

In the model, the borehole was in deep rock and surrounded by rocks that may be regarded as an infinite medium. Non-reflective boundary conditions were applied to the top, bottom, rear, and two

sidewall surfaces of the model. The rear surface and two sides of the model were fixed to simulate the effects of clipping by the surrounding rock. A circumferential pressure was applied on the borehole inner walls through the high-pressure rubber sleeve. Data were collected for every 1-MPa increase in pressure until the appearance of a tensile stress zone in the model. The Mohr-Coulomb yield criterion was used in the computation of the model [13,23,34]:

$$f^s = \sigma_1 - \sigma_3 \frac{1 + \sin\phi}{1 - \sin\phi} + 2c\sqrt{\frac{1 + \sin\phi}{1 - \sin\phi}} \qquad (18)$$

where f^s is the shear yield function; σ_1 and σ_3 are the maximum and minimum principal stresses (MPa), respectively; c is the bonding strength of the material (MPa); and φ is the internal friction angle of the rock (°).
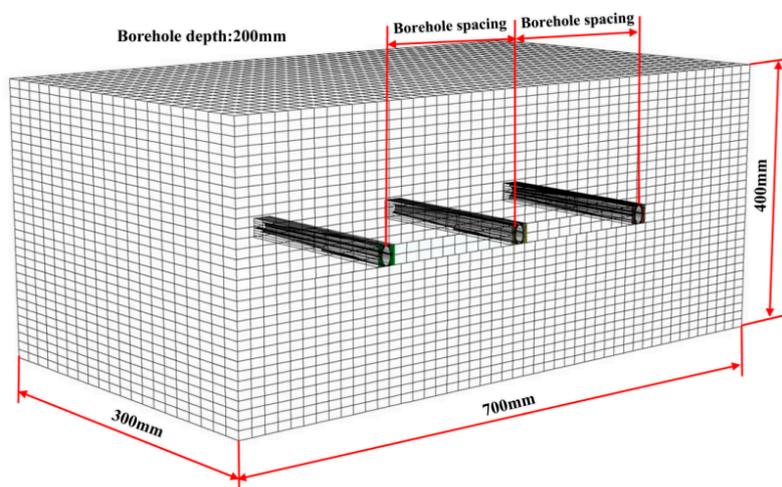
Figure 2. Three-dimensional model of sleeve fracturing of hard roof.

Table 1. Measured physical and mechanical parameters of sandstone in experiments [13].

Type	Compressive Strength (MPa)	Tensile Strength (MPa)	Cohesive Strength (MPa)	Internal Friction Angle (°)	Modulus of Elasticity (GPa)	Poisson's Ratio (μ)	Density (kg·m^{-3})
Sandstone	21.00	0.91	0.93	45	4.00	0.23	2600

3.2. Results

3.2.1. Model 1

For model 1, when the hole spacing was 5*d* and the sleeve pressure was 14 MPa, the maximum stress value was 15.1 MPa, which was located on the left and right sides of the hole. The maximum compressive stress was 15.3 MPa, which was located on the top and bottom of the hole. At this time, a tensile stress zone appeared at the contour value of 7.70 MPa, which exceeded the tensile strength of the rock. It was determined that the rock had already cracked in the direction of the row of holes (Figure 3a). Similarly, the destructive pressure was 19 MPa with a hole spacing of 8*d* when a tensile stress zone appeared between the holes at the contour value of 2.84 MPa. Cracks propagated in the direction of the row of holes. In addition, there were tensile stress zones in the direction orthogonal to the second borehole (Figure 3b). When the hole spacing was 10*d*, the destructive pressure was 26 MPa. There were tensile stress values exceeding the tensile stress of the rocks on both the top and bottom of the borehole. There were cracks from the top to the bottom, crossing the borehole in the model (Figure 3c).
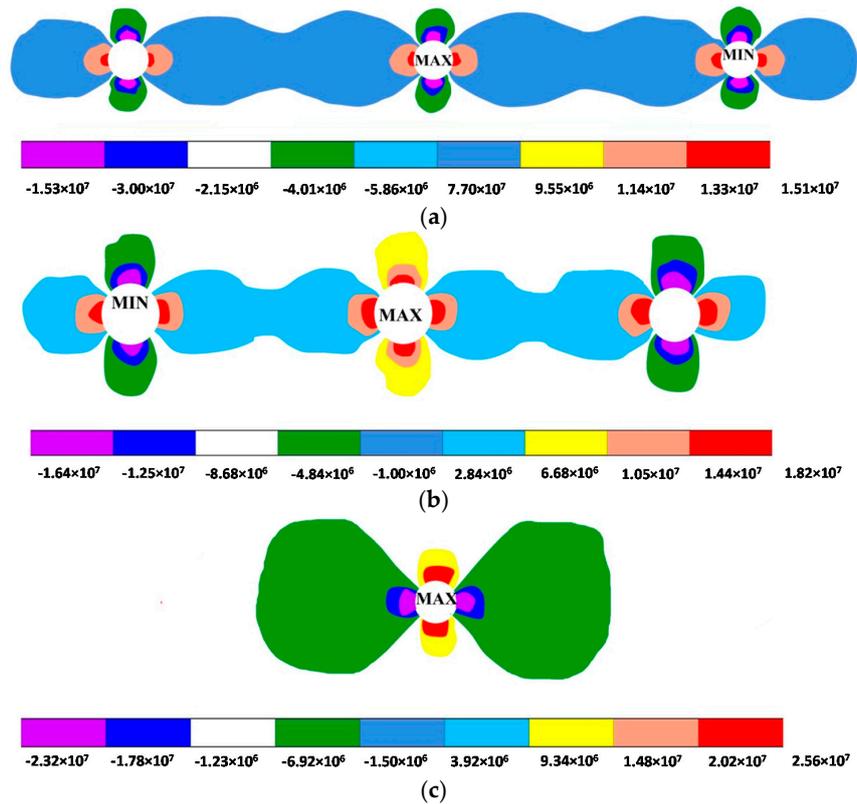
Figure 3. Pressure cloud images for model 1. (**a**) Hole spacing of 5*d* and sleeve pressure of 14 MPa; (**b**) Hole spacing of 8*d* and sleeve pressure of 19 MPa; (**c**) Hole spacing of 10*d* and sleeve pressure of 26 Mpa.

3.2.2. Model 2

For model 2, when the hole spacing was 5*d* and the sleeve pressure was 14 MPa, the maximum stress value was 12.0 MPa, which was located on the left and right sides of the hole. The maximum compressive pressure was 12.2 MPa, which was located on the top and bottom of the hole. At this time, a tensile stress zone appeared at the contour value of 1.24 MPa, which exceeded the tensile strength of the rock. It was determined that the rock had already cracked in the direction of the row of holes (Figure 4a). When the hole spacing was 8*d*, the model cracked in the direction of the row of holes, where a 1.24-MPa tensile stress zone appeared under a sleeve pressure of 17 MPa (Figure 4b). When the hole spacing was 10*d* and the sleeve pressure was 21 MPa, a 3.63-MPa tensile stress zone appeared along the row of holes, and the crack expanded in the same direction (Figure 4c).
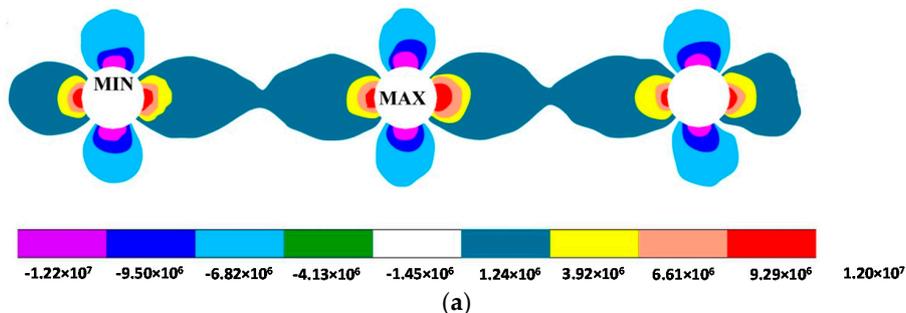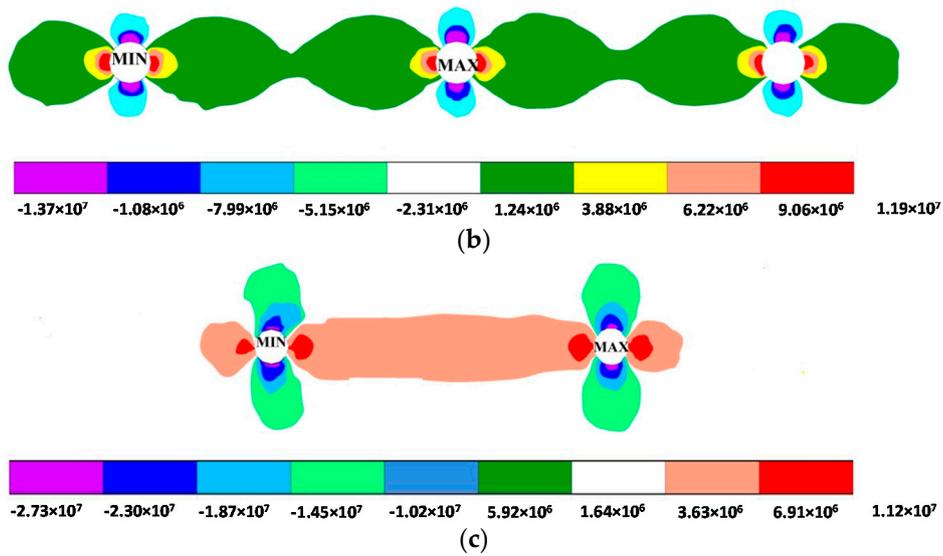

Figure 4. *Cont.*

(b)

(c)

Figure 4. Pressure cloud images for model 2. (**a**) Hole spacing of 5*d* and sleeve pressure of 14 MPa; (**b**) Hole spacing of 8*d* and sleeve pressure of 17 MPa; (**c**) Hole spacing of 10*d* and sleeve pressure of 21 MPa.

3.2.3. Model 3

For model 3, when the hole spacing was 5*d* and the sleeve pressure was 12 MPa, the maximum stress value was 12.0 MPa, which was located on the left and right sides of the hole. The maximum compressive pressure was 12.2 MPa, which was located on the top and bottom of the hole. A 1.66-MPa tensile stress zone appeared between the boreholes, which exceeded the tensile strength of the rock. The model cracked along the row of holes. In addition, there were tensile stress zones orthogonal to the second borehole, and cracks also developed (Figure 5a). When the hole spacing was 8*d*, a 0.73-MPa tensile stress zone appeared, and the model cracked along the row of holes under a 15-MPa sleeve pressure (Figure 5b). When the hole spacing was 10*d* and the sleeve pressure was 20 MPa, a 4.00-MPa tensile stress zone appeared, and cracks expanded along the row of holes (Figure 5c).
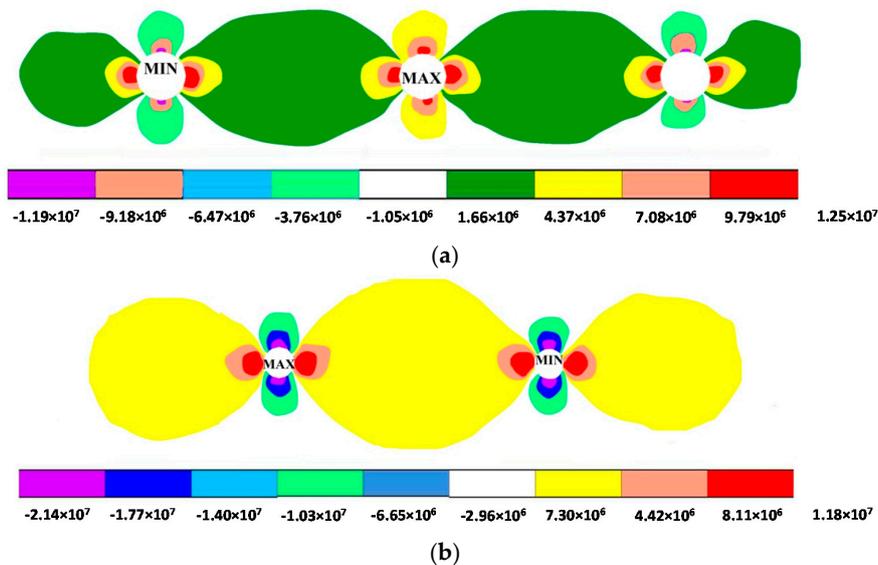

(a)

(b)

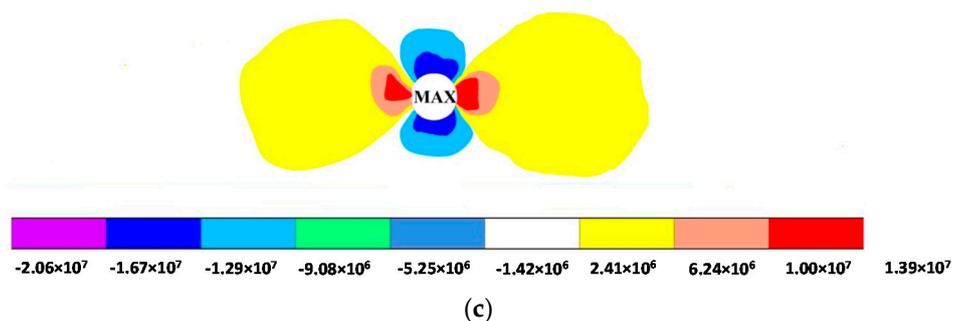**Figure 5.** *Cont.*

(c)

Figure 5. Pressure cloud images for model 3. (**a**) Hole spacing of 5*d* and sleeve pressure of 12 MPa; (**b**)Hole spacing of 8*d* and sleeve pressure of 15 MPa; (**c**) Hole spacing of 10*d* and sleeve pressure of 20 MPa.

4. Experiment on Cracking Roof with SFM

4.1. Method

This experiment was conducted at the Engineering Research Center of Underground Engineering, Ministry of Education, Anhui University of Science and Technology in Huainan, Anhui Province. Cement mortar was used as a material similar to rock to fabricate experimental models with the dimensions of 700 mm × 300 mm × 400 mm [17,35,36]. Based on Froude's similarity law, a similarity ratio of 10 was used for the parameters of similar materials, according to Table 1 [2,37]. The experiments were divided into three large groups, with values of 20, 30 and 40 mm used for diameter *d*. Each diameter group was further divided into three subgroups according to the hole spacing (5*d*, 8*d* and 10*d*). The hole depth was fixed at 200 mm.

During the experiment, data were manually collected at the stable state for every 1 MPa increase in the pump pressure until the test piece was destroyed, and the final destruction pressure was recorded.

4.2. Experiment Results

4.2.1. Similar Model 1

In similar model 1, the borehole diameter *d* was 20 mm, and the borehole depth was 200 mm. The sleeve fracturing pressures under the different hole spacing configurations are listed in Table 2.

Table 2. Sleeve fracturing pressures under different hole spacing configurations in model 1.

Measured Values	Borehole Spacing (mm)		
	100	**160**	**200**
Sleeve Fracturing Pressure (MPa)	13.8	18.4	23.6

The model cracked when the borehole spacing was 5*d* and the sleeve pressure was 13.8 MPa. Cracks developed along the row of holes, and the strain gauges at points 1–5 were broken by pulling. The model also cracked when the borehole spacing was 8*d* and the sleeve pressure was 18.4 MPa. Cracks developed around a "+"shaped central hole, and became wider in the direction orthogonal to the row of holes. When the borehole spacing was 10*d* and the sleeve pressure was 23.6 MPa, the model cracked and the strain gauges at points 2, 4 and 7 were broken by pulling (Figure 6b).
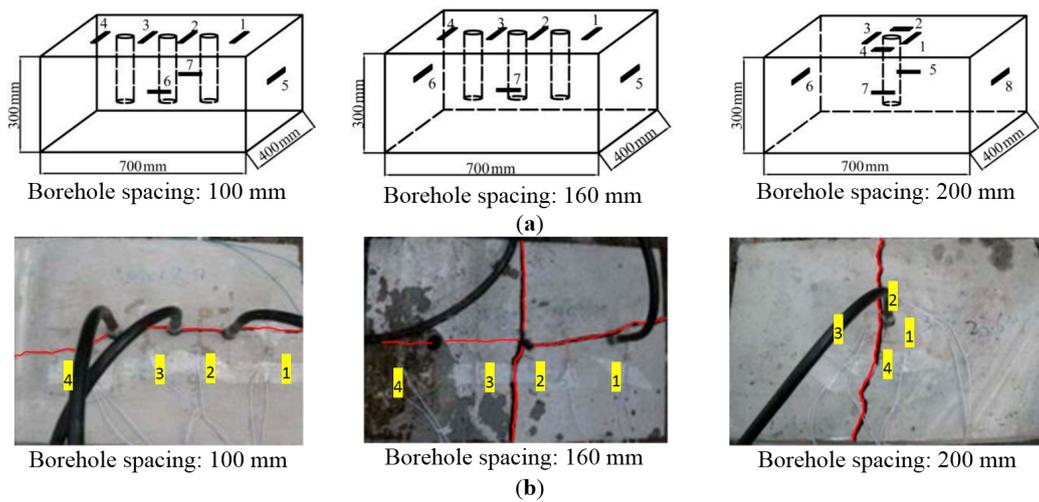
Figure 6. Strain gauge distribution and effects in model 1 after fracturing experiment. (**a**) Strain gauge distribution; (**b**) Roof fracturing experiment.

4.2.2. Similar Model 2

In similar model 2, the borehole diameter *d* was 30 mm and the borehole depth was 200 mm. The sleeve fracturing pressures under different hole spacing configurations are listed in Table 3.

Table 3. Sleeve fracturing pressures under different hole spacing configurations in model 2.

Measured Values	Borehole Spacing (mm)		
	150	240	300
Sleeve Fracturing Pressure (MPa)	10.6	16.7	20.4

When the borehole spacing values were 5*d*, 8*d* and 10*d*, the sleeve pressures at which the model was destroyed were 10.6, 16.7 and 20.4 MPa, respectively. Cracks extended along the direction of the row of holes (Figure 7b).
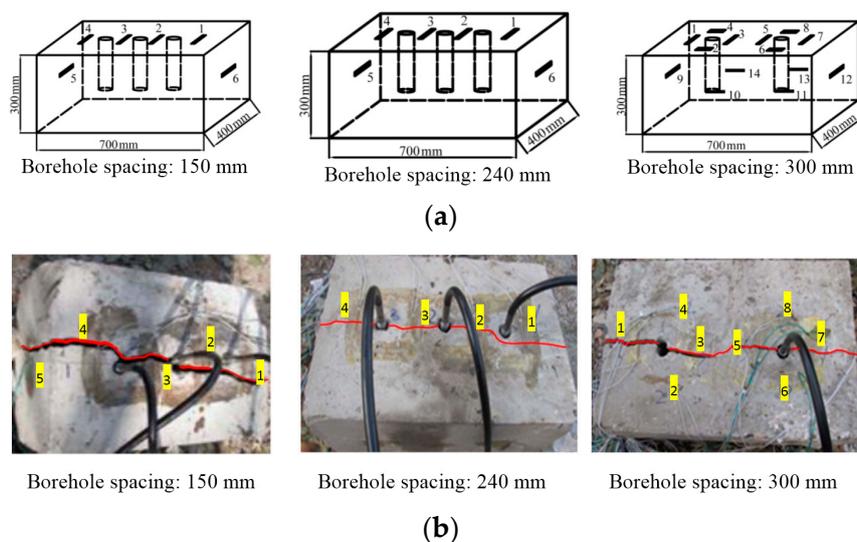

Figure 7. Strain gauge distribution and effects in model 2 after fracturing experiment. (**a**) Strain gauge distribution; (**b**) Roof fracturing experiment.

4.2.3. Similar Model 3

In similar model 3, the borehole diameter *d* was 40 mm and the borehole depth was 200 mm. The sleeve fracturing pressures under different hole spacing configurations are listed in Table 4.

Table 4. Sleeve fracturing pressures under different hole spacing configurations in model 3.

Measured Values	Borehole Spacing (mm)		
	200	320	400
Sleeve Fracturing Pressure (MPa)	9.2	10.7	17.6

When the borehole spacing was 5*d* and the sleeve pressure was 9.2 MPa, the model cracked in the middle, and the cracks developed in a "+" shape. The crossing of the cracks did not pass the borehole. When the hole spacing was 8*d*, the model cracked along the row of holes under a sleeve pressure of 10.7 MPa. However, the strain gauge at point 3 was not destroyed. When the hole spacing was 10*d*, the model was destroyed at a sleeve pressure of 17.6 MPa. The cracks developed along the long sides of the model, indicating that the fracturing pressure was not influenced by the boundary conditions (Figure 8b).
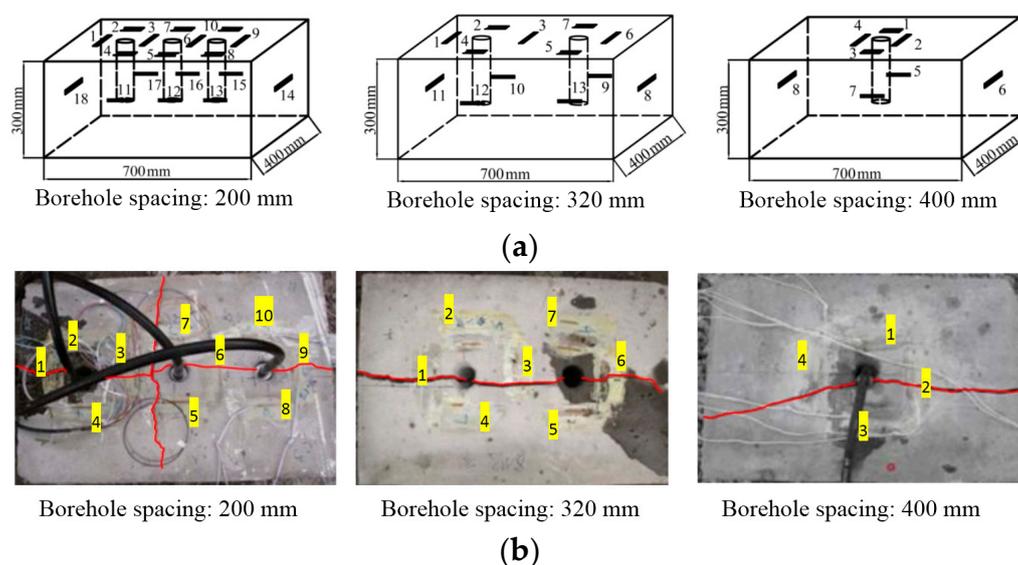

Borehole spacing: 200 mm   Borehole spacing: 320 mm   Borehole spacing: 400 mm

(**a**)

Borehole spacing: 200 mm   Borehole spacing: 320 mm   Borehole spacing: 400 mm

(**b**)

Figure 8. Strain gauge distribution and effects in model 3 after fracturing experiment. (**a**) Strain gauge distribution; (**b**) Roof fracturing experiment.

5. Discussion

The SFM is mainly applied to ground stress measurement. In this method, high-pressure oil is injected into a hollow rubber sleeve, through which pressure is loaded onto the borehole sidewall to crack the surrounding rocks. This method was used to weaken the hard roof of a deep mine in this research. Compared to the traditional blasting weakening method, the SFM does not generate strong blasting shocks and toxic gases. In contrast to the high-pressure water fracturing method, it is not constrained by the construction environment. In order to explore the feasibility of the SFM, simulation analyses were conducted using the numerical analysis software FLAC^{3D}, and similar models were used to validate the results.

5.1. Similar Model 1

When the hole spacing was 100 mm, the strain value was very small, and the growth rate was slow in the initial stage of the experiment. At a pressure of 8 MPa, a strain started to develop at point 2. With increases in pressure, the growth rate increased, along with the strains at points 1, 3 and 5. When the pressure reached 13.8 MPa, the test piece cracked, and the strain gauges at points 1–5 were broken by pulling. The strain at point 2 was the highest at 929$\mu\varepsilon$, and that at point 4 was the lowest at 109 $\mu\varepsilon$. Then, the gauge was suddenly broken by pulling. When the hole spacing was 160 mm, the strains surrounding the borehole were quickly redistributed in the initial stage of the experiment. There were relatively large fluctuations at points 1 and 2, while the other points experienced very little change. When the pressure was 11 MPa, the strain at point 7 started to increase slowly. When the pressure reached 16 MPa, the strains at points 2, 4 and 5 increased quickly. At a pressure of 18.4 MPa, the strain gauge at point 7 was broken by pulling, and the maximum strain was 337 $\mu\varepsilon$. When the hole spacing was 200 mm, the strain curve at point 2 was pronounced. The strain gradually increased with the sleeve pressure. When the strain reached 911 $\mu\varepsilon$, the test piece was destroyed when the sleeve pressure reached 23.6 MPa. There were obvious changes at points 4 and 7 when the pressure reached 19 MPa. When the pressure reached 23.6 MPa, the gauge at point 7 was broken by pulling. A strain recovery process occurred at point 4 after the test piece was destroyed (Figure 9a).

5.2. Similar Model 2

When the hole spacing was 150 mm, there were small changes in the strains at all the points before the pressure reached 4 MPa, after which there were noticeable changes in the strain curves at points 2–4. The strain gradually increased with the sleeve pressure. The test piece was destroyed at a sleeve pressure of 10.6 MPa. When the hole spacing was 240 mm, there were small changes in the strains at the points in the initial stage of the experiment. After the pressure reached 9 MPa, the strain curve at point 2 was pronounced. The strains at points 1 and 6 also gradually increased with the sleeve pressure. The test piece was destroyed at a sleeve pressure of 16.7 MPa. At this time, the strain gauges at points 1, 2 and 6 were broken by pulling. When the hole spacing was 300 mm, the strains at points 1, 3 and 9 were pronounced, and the highest strain was 717 $\mu\varepsilon$. The model was destroyed when the sleeve pressure reached 20.4 MPa (Figure 9b).

5.3. Similar Model 3

When the hole spacing was 200 mm, the strains at all the measuring points changed very slowly in the initial stage of the experiment, and started to increase after the sleeve pressure reached 4 MPa. After 5 MPa, the strains at points 1 and 2 started to increase rapidly, while there was a negative strain at point 12. The test piece was destroyed when the sleeve pressure reached 9.2 MPa, and the strain gauges at points 1, 3, 6, 9, 14, 16 and 18 were broken. Point 1 had the highest strain at 893 $\mu\varepsilon$, and point 12 had the lowest strain at −298 $\mu\varepsilon$, which was compressive. When the hole spacing was 320 mm, the strains at all the measuring points changed very slowly in the initial stage. The test piece was successfully fractured at a pressure of 10.7 MPa, and cracks developed along the designed direction. At this time, the gauges at points 1, 6 and 8 were broken by pulling because they were along the direction of cracking. The crack also passed point 3, and the measured strain was 732 $\mu\varepsilon$. The strains measured at the sides of the hole at points 2, 7 and 12 were all negative (compressive). When the hole spacing was 400 mm, the strains at all the points were very small in the initial stage. The test piece was destroyed when the sleeve pressure reached 17.6 MPa, and the gauges at points 4 and 8 were broken by pulling. The maximum strain was 1156 $\mu\varepsilon$ at point 4, while strains at all the other sites were very small. The cracks developed along the long sides of the model, which indicated that the fracturing pressure was not influenced by the boundary conditions (Figure 9c).
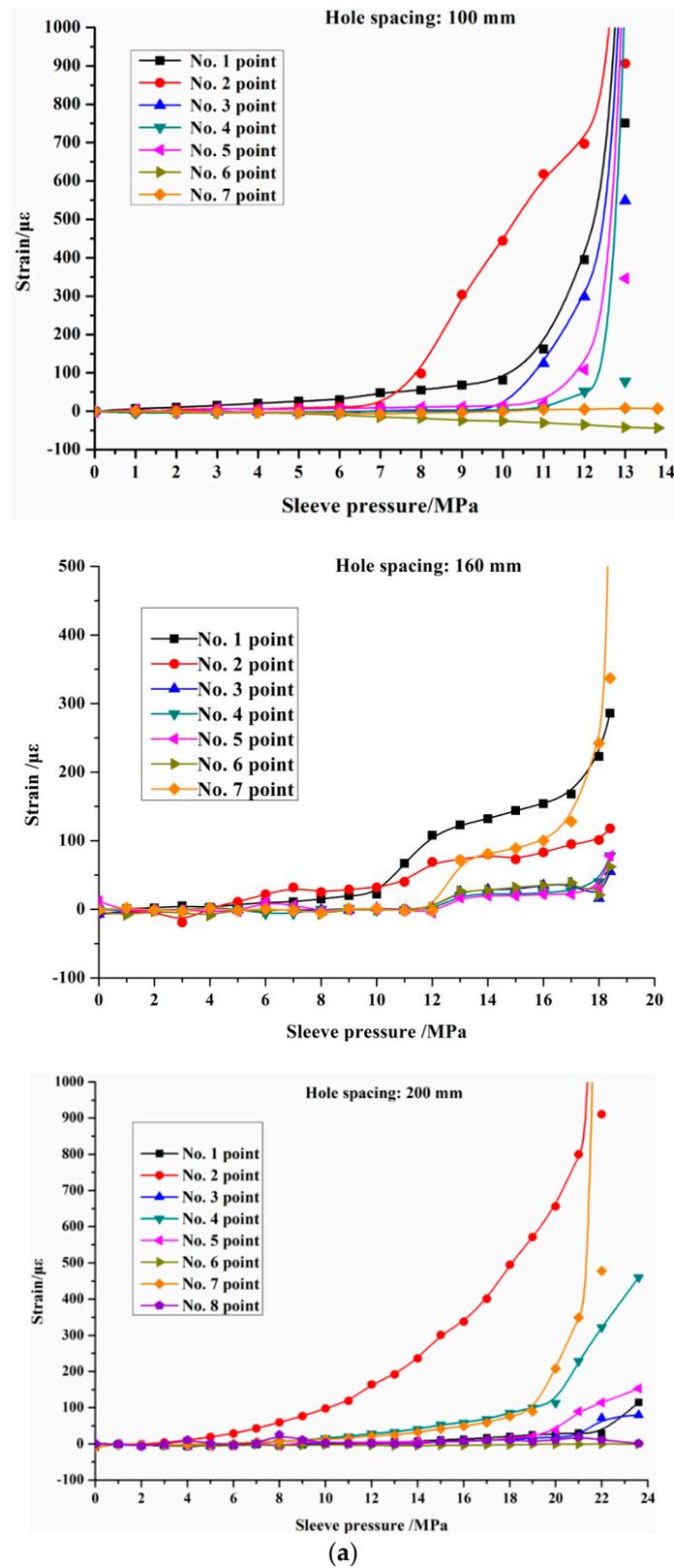
Figure 9. *Cont.*
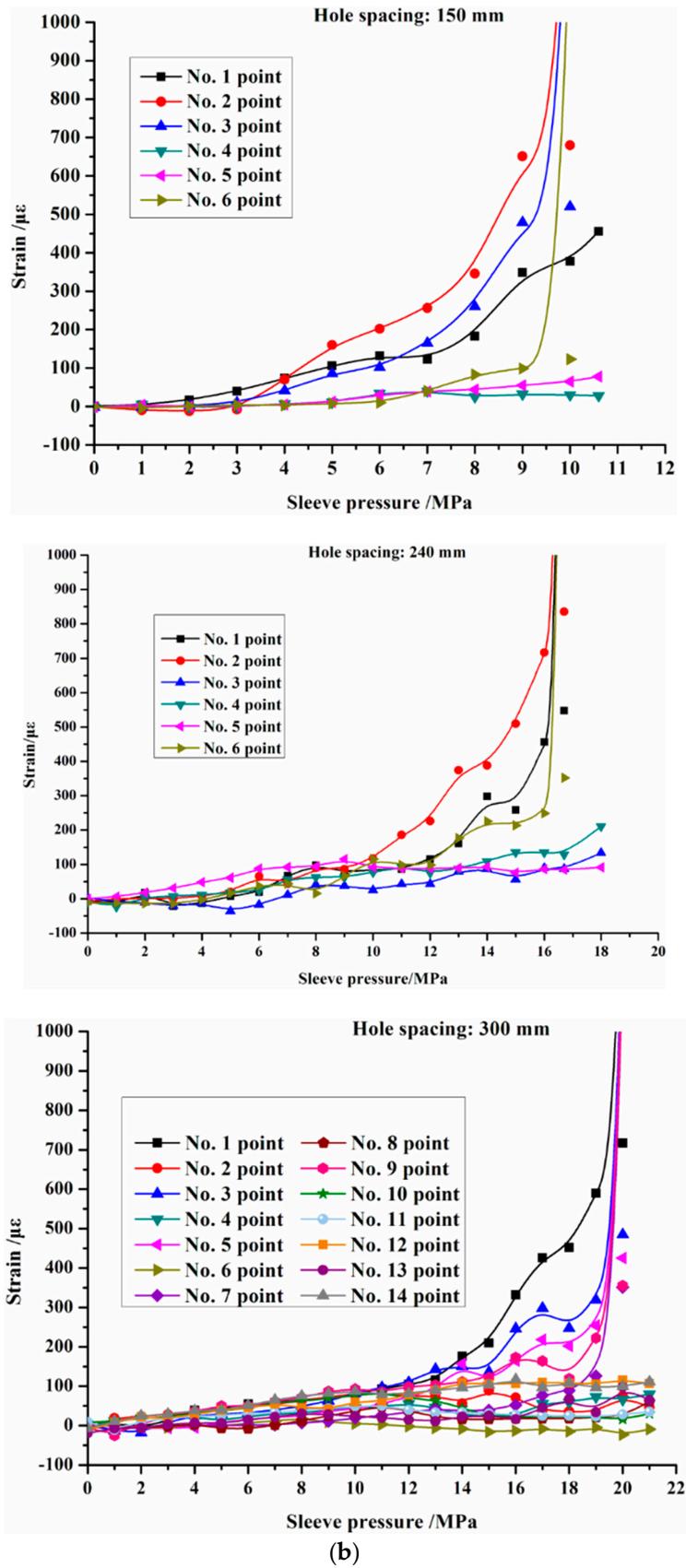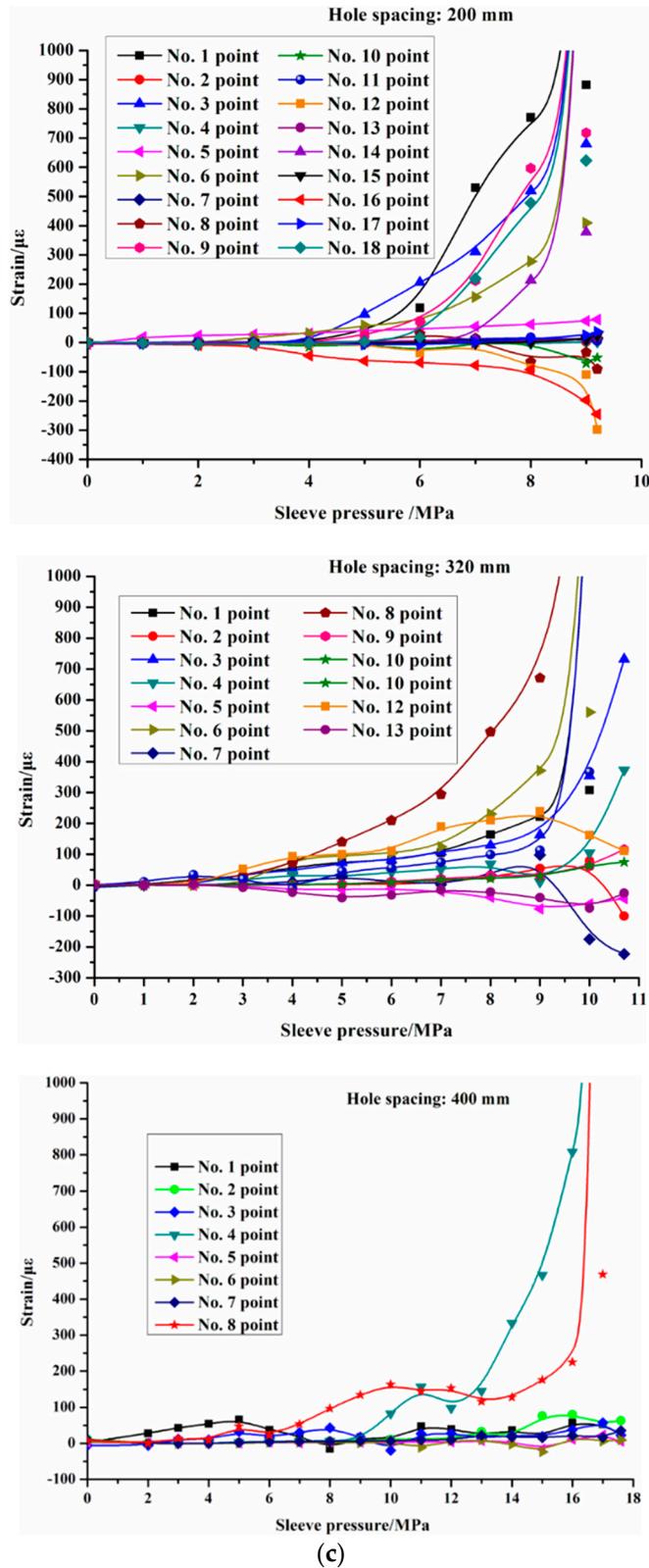
Figure 9. *Cont.*

Figure 9. Relationship between sleeve pressure and strain. (**a**) Similar model 1; (**b**) Similar model 2; (**c**) Similar model 3.

After the destruction of the similar model, cracks extended toward the row of holes. From the analyses of the numerical simulation and experimental results for the sleeve fracturing of hard

roofs, it was determined that boreholes have a certain guiding role in the direction of cracking. The boreholes formed weak sides inside the model. When a circumferential pressure was applied on the inner sidewall of the boreholes inside the model, the destruction of the model began at the weak sides. Huang *et al.* [27] used a large three-axis hydraulic fracturing experiment system and three-dimensional positioning system for acoustic emission to study the crack propagation law and boreholes under hydraulic fracturing. Their results indicated that the boreholes were stress-concentration areas. The test piece was destroyed along the row of holes, and cracks extended outward from the boreholes. As shown in Figure 6b, when the hole spacing was 160 mm, a "+"shaped crack appeared in the middle hole of the model. The mechanism of the single-hole UCF revealed that this was mainly due to the stress superposition of the two edge holes at the center hole. As shown in Figure 8b, when the hole spacing was 200 mm, a "+"shaped crack developed in the middle of the model. However, the crossing of the cracks did not pass the borehole because of the gaps inside the model.

The abovementioned analysis revealed that rock fracturing effects are related to various factors such as the borehole diameter, hole spacing, and sleeve pressure in the process of hard-roof weakening in mines. The relationships between the borehole diameter, hole spacing, and sleeve fracturing pressure for the three models were summarized based on the results of numerical analyses and experiments and are shown in Figure 10 (Diameter ratio is the ratio of the hole spacing and hole diameter).
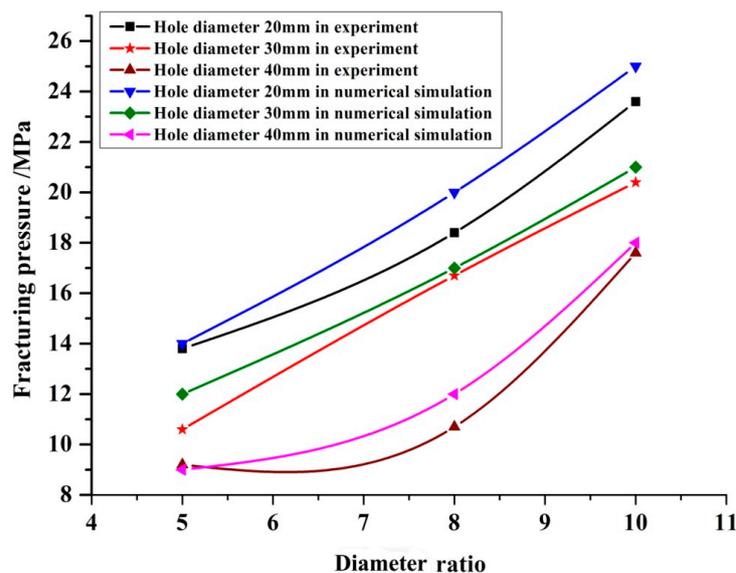

Figure 10. Comparison of fracturing pressures in three models.

In either the numerical analyses or the experiments, with the same borehole diameter, the sleeve pressure needed for the destruction of the model increased with an increase in the hole spacing (Figure 10). Hence, the borehole spacing must be designed according to the influence range of the sleeve pressure, and should be less than the influence radius of the sleeve pressure [31]. An extremely small borehole spacing will increase the borehole work load, which is not economical because it increases the human and material resource costs in practical engineering. Therefore, a borehole spacing of *10d* should be selected. Under the same diameter ratio, the fracturing pressure was the highest for the model with a diameter of 20 mm, while it was the lowest for that with a diameter of 40 mm. This is explained by the fact that rocks with a larger cross-sectional area for the weak sides are easier to destroy. Huang *et al.* [17] used the developed high-pressure water fracturing equipment in multi-hole water fracturing and deep-water fracturing experiments. The size of the cement-mortar model test piece was 300 mm × 300 mm × 300 mm. The measured

water pressures for destroying models with borehole diameters of 10, 15 and 20 mm were 10.2, 9.1 and 7.8 MPa, respectively, which agreed with the results of this research. The experiment results showed that longer cracks could be obtained in the model with 40-mm-diameter boreholes under the lowest sleeve pressure, and the direction of the developing cracks was easy to control. In addition, Charsley *et al.* [30] pointed out that high-pressure rubber sleeves with a larger diameter can withstand greater deformation and are not easily damaged. Therefore, it may be easier for a small-diameter sleeve to burst. Hence, a borehole diameter of 40 mm should be selected. Overall, the sleeve fracturing pressures in the numerical simulations were higher than those in the experimental models. This was because the selected materials were ideally uniform in the numerical simulation, whereas air could have been present in the materials used in the experiments. There was also a certain dispersion in the experimental data of the models. Summarizing all of the above results, the most ideal fracturing effect was found when the borehole diameter was 40 mm, the hole spacing of the model was 400 mm, and the sleeve fracturing pressure was 17.6 MPa. The findings of this research will be useful for studies on hard-roof weakening [2,13,19].

In this study, numerical analyses and experimental methods were used to validate the feasibility of applying sleeve fracturing technology to hard-roof weakening. This technology has little influence on the stability of the surrounding rock. It has a wide range of applications. It could effectively control hard roof caving and reduce the occurrence probability of mine disasters, including the impact of ground pressure, hurricanes, and gas outbursts. It has the ability to ensure the safety of construction personnel and equipment, and allow the mine production to be carried out safely and effectively.

However, the time, creep effect of rocks under high pressure, and influence of the depth of the drilling holes on the cracks were not taken into account in this study, which could be viewed as shortcomings.

6. Conclusions

A few of the drawbacks of other methods could be overcome by applying the SFM to hard-roof weakening at the FMMF of a deep mine. For instance, the strong shock effects on the surrounding rocks of the traditional blasting weakening method and the constraints of the hydraulic fracturing method could be avoided. The following can be concluded from the FLAC^{3D} simulation analyses and similar model test results: (1) the multi-hole controlled SFM can be used to control the crack propagation direction, which is affected by the maximum principal stress and hole spacing. The fracturing effects are influenced by various factors, including the borehole diameter, hole spacing, and sleeve pressure. When the borehole diameter is fixed, fracturing pressure increases with an increase in the hole spacing; (2) When the fracturing pressure is fixed, the fracturing range increases with an increase in the borehole diameter. Overall, the results of the simulation analyses agreed with the results of the experiment models. The fracturing pressure was the lowest in the model when the borehole diameter was 40 mm and the hole spacing was 400 mm. The obtained cracks were the longest, and the direction of cracking was easy to control. The results of this study have important theoretical significance and can be applied to the exploration of new methods for hard-roof weakening to allow safe and fast construction in deep mines.

Author Contributions: Y.X. and J.D. conceived and designed the experiments; Z.Z. performed the experiments; Z.Z. and D.L. analyzed the data; Z.Z., Y.X. and J.D. wrote the paper.

Conflicts of Interest: The authors declare no conflict of interest.

References

1. Zhang, B.; Cao, S. Study on first caving fracture mechanism of overlying roof rock in steep thick coal seam. *Int. J. Min. Sci. Technol.* **2015**, *25*, 133–138. [CrossRef]

2. Lu, C.P.; Dou, L.M.; Zhang, N.; Xue, J.H.; Wang, X.N.; Liu, H.; Zhang, J.W. Microseismic frequency-spectrum evolutionary rule of rockburst triggered by roof fall. *Int. J. Rock Mech. Min. Sci.* **2013**, *64*, 6–16. [CrossRef]

3. Baghbanan, A.; Jing, L. Stress effects on permeability in a fractured rock mass with correlated fracture length and aperture. *Int. J. Rock Mech. Min. Sci.* **2008**, *45*, 1320–1334. [CrossRef]

4. Alehossein, H.; Poulsen, B.A. Stress analysis of longwall top coal caving. *Int. J. Rock Mech. Min. Sci.* **2010**, *45*, 30–41. [CrossRef]

5. Wang, X.; Xu, J.; Zhu, W.; Li, Y. Roof pre-blasting to prevent support crushing and water inrush accidents. *Int. J. Min. Sci. Technol.* **2012**, *22*, 379–384. [CrossRef]

6. Ouyang, Z. Mechanism and Experiment of Hydraulic Fracturing in Rock Burst Prevention. In Proceedings of the 1st International Conference on Rock Dynamics and Applications, Lausanine, Switzerland, 5 June 2013; pp. 245–250.

7. Li, Q.; Lin, B.; Zhai, C. A new technique for preventing and controlling coal and gas outburst hazard with pulse hydraulic fracturing: A case study in Yuwu coal mine, China. *Nat. Hazards* **2015**, *75*, 2931–2946. [CrossRef]

8. Dou, L.M.; He, X.Q.; He, H.; He, J.; Fan, J. Spatial structure evolution of overlying strata and inducing mechanism of rockburst in coal mine. *Trans. Nonferr. Met. Soc. China* **2014**, *24*, 1255–1261. [CrossRef]

9. Adoko, A.C.; Gokceoglu, C.; Wu, L.; Zuo, Q.J. Knowledge-based and data-driven fuzzy modeling for rockburst prediction. *Int. J. Rock Mech. Min. Sci.* **2013**, *61*, 86–95. [CrossRef]

10. Xie, Z.; Cai, J.; Zhang, Y. Division of spontaneous combustion "three-zone" in goaf of fully mechanized coal face with big dip and hard roof. *Procedia Eng.* **2012**, *43*, 82–87. [CrossRef]

11. Tan, Y.; Zhao, T.; Xiao, Y. Quantitative prop support estimation and remote monitor early warning for hard roof weighting at the Muchengjian Mine in China. *Can. Geotech. J.* **2010**, *47*, 947–954. [CrossRef]

12. Konicek, P.; Soucek, K.; Stas, L.; Singh, R. Long-hole destress blasting for rockburst control during deep underground coal mining. *Int. J. Rock Mech. Min. Sci.* **2013**, *61*, 141–153. [CrossRef]

13. Hongbao, Z. Numerical simulation on pressure behavior of mining field under the conditions of hard roof. *Disaster Adv.* **2011**, *4*, 15–20.

14. Ito, T.; Hayashi, K. Physical background to the breakdown pressure in hydraulic fracturing tectonic stress measurements. *Int. J. Rock Mech. Min. Sci. Geomech. Abstr.* **1991**, *28*, 285–293. [CrossRef]

15. Fan, J.; Dou, L.; He, H.; Du, T.; Zhang, S.; Gui, B.; Sun, X. Directional hydraulic fracturing to control hard-roof rockburst in coal mines. *Int. J. Min. Sci. Technol.* **2012**, *22*, 177–181. [CrossRef]

16. Wang, F.; Tu, S.; Yuan, Y.; Feng, Y.; Chen, F.; Tu, H. Deep-hole pre-split blasting mechanism and its application for controlled roof caving in shallow depth seams. *Int. J. Rock Mech. Min. Sci.* **2013**, *64*, 112–121. [CrossRef]

17. Huang, B.X.; Wang, Y.Z.; Cao, S.G. Cavability control by hydraulic fracturing for top coal caving in hard thick coal seams. *Int. J. Rock Mech. Min. Sci.* **2015**, *74*, 45–57. [CrossRef]

18. Wang, W.; Cheng, Y.P.; Wang, H.F.; Liu, H.Y.; Wang, L.; Li, W.; Jiang, J.Y. Fracture failure analysis of hard–thick sandstone roof and its controlling effect on gas emission in underground ultra-thick coal extraction. *Eng. Fail. Anal.* **2015**, *54*, 150–162. [CrossRef]

19. Li, C.R.; Kang, L.J.; Qi, Q.X.; Mao, D.B.; Liu, Q.M.; Xu, G. The numerical analysis of borehole blasting and application in coal mine roof-weaken. *Proced. Earth Planet. Sci.* **2009**, *1*, 451–459.

20. He, H.; Dou, L.; Fan, J.; Du, T.; Sun, X. Deep-hole directional fracturing of thick hard roof for rockburst prevention. *Tunn. Underg. Space Technol.* **2012**, *32*, 34–43. [CrossRef]

21. Zang, C.W.; Zhuang, X.; Ma, C.L. Research of large-area hard roof caving prevention and control system in shortwall mining face. *Adv. Mater. Res.* **2013**, *734*, 802–808. [CrossRef]

22. Lu, C.-P.; Liu, G.-J.; Liu, Y.; Zhang, N.; Xue, J.-H.; Zhang, L. Microseismic multi-parameter characteristics of rockburst hazard induced by hard roof fall and high stress concentration. *Int. J. Rock Mech. Min. Sci.* **2015**, *76*, 18–32. [CrossRef]

23. Pan, C.; Zuo, Y.J.; Gao, S.; Li, W. Numerical simulation on hard and stable roof control by means of directional hydraulic fracturing in coal mine. *Appl. Mech. Mater.* **2014**, *638*, 894–897. [CrossRef]

24. Baghbanan, A.; Jing, L.R. Hydraulic properties of fractured rock masses with correlated fracture length and aperture. *Int. J. Rock Mech. Min. Sci.* **2007**, *44*, 704–719. [CrossRef]

25. Yang, H.; Wang, R.; Zhou, W.; Li, L.; Chen, F. A study of influencing factors on fracture initiation pressure of cemented sliding sleeve fracturing. *J. Nat. Gas Sci. Eng.* **2014**, *18*, 219–226. [CrossRef]

26. Ljunggren, C.; Stephansson, O. Sleeve fracturing-a borehole technique for in-situ determination of rock deformability and rock stresses. In Proceedings of the in International Society for Rock Mechanics, Stockholm, Sweden, 31 August–3 September 1986.

27. Huang, B.; Li, P.; Ma, J.; Chen, S. Experimental investigation on the basic law of hydraulic fracturing after water pressure control blasting. *Rock Mech. Rock Eng.* **2014**, *47*, 1321–1334. [CrossRef]

28. He, L.; An, X.M.; Ma, G.W.; Zhao, Z.Y. Development of three-dimensional numerical manifold method for jointed rock slope stability analysis. *Int. J. Rock Mech. Min. Sci.* **2013**, *64*, 22–35. [CrossRef]

29. Irwin, G.R. Analysis of stresses and strains near the end of a crack traversing a plate. *J. Appl. Mech.* **1957**, *24*, 361–364.

30. Charsley, A.D.; Martin, C.D.; McCreath, D.R. Sleeve-fracturing limitations for measuring *in situ* stress in an anisotropic stress environment. *Int. J. Rock Mech. Min. Sci.* **2003**, *40*, 127–136. [CrossRef]

31. Brenne, S.; Molenda, M.; Stockhert, F.; Alber, M. Hydraulic and sleeve fracturing laboratory experiments on 6 rock types. In Proceedings of the International Society for Rock Mechanics International Conference for Effective and Sustainable Hydraulic Fracturing, Brisbane, Australia, 20–22 May 2013.

32. Huang, B.; Liu, C.; Fu, J.; Guan, H. Hydraulic fracturing after water pressure control blasting for increased fracturing. *Int. J. Rock Mech. Min. Sci.* **2011**, *48*, 976–983. [CrossRef]

33. Griffith, A.A. The phenomena of rupture and flow in solids. *Philos. Trans. R. Soc. Lond.* **1921**, *221*, 163–198. [CrossRef]

34. Li, N.; Wang, E.Y.; Ge, M.C.; Liu, J. The fracture mechanism and acoustic emission analysis of hard roof: A physical modeling study. *Arab. J. Geosci.* **2015**, *8*, 1895–1902. [CrossRef]

35. Zhang, G.Q.; Fan, T. A high-stress tri-axial cell with pore pressure for measuring rock properties and simulating hydraulic fracturing. *Measurement* **2014**, *49*, 236–245. [CrossRef]

36. Tan, Y.; Yu, F.; Ning, J.; Zhao, T. Design and construction of entry retaining wall along a gob side under hard roof stratum. *Int. J. Rock Mech. Min. Sci.* **2015**, *77*, 115–121. [CrossRef]

37. Congliang, L.; Tan, Z.; Deng, K.; Li, P. Synergistic instability of coal pillar and roof system and filling method based on plate model. *Int. J. Min. Sci. Technol.* **2013**, *23*, 145–149. [CrossRef]